Journal of Solid State Chemistry 182 (2009) 1806–1820

Contents lists available at ScienceDirect

Journal of Solid State Chemistry

journal homepage: www.elsevier.com/locate/jssc

Polymorphism of the iron doped strontium aluminate $SrAl_{1.5}Fe_{0.5}O_4$

H. Desmoulins, S. Malo *, S. Boudin, V. Caignaert, M. Hervieu

Laboratoire CRISMAT-ENSICAEN, Bd du Maréchal Juin-14050 CAEN, Cedex, France

ARTICLE INFO

Article history:
Received 16 January 2009
Received in revised form
3 April 2009
Accepted 5 April 2009
Available online 22 April 2009

Keywords:
Tridymite derivative structures
Transmission electron microscopy
Ferri-aluminates
Thermal analysis

ABSTRACT

The partial substitution of Al by Fe atoms in $SrAl_2O_4$ allowed to stabilize four stuffed tridymite derivative structures $SrAl_{1.5}Fe_{0.5}O_4$. The different phases have been characterized by TEM and XRPD techniques. Two are isotypes of those observed for the undoped oxides, namely the hexagonal phase with $\sqrt{3}A \times \sqrt{3}A \times C$ (with A and C being the tridymite unit cell parameters) and space group $P6_3$ and the monoclinic one with $A \times \sqrt{3}A \times C$, $\beta \approx 93^\circ$ and space group $P2_1$, with a synthesis temperature lower than the one required for $SrAl_2O_4$. By annealing, two original phases, denoted O_1 and O_2, are obtained; they are metrically similar ($3A \times \sqrt{3}A \times C$ and $\beta \approx 90^\circ$) and only differ by their space groups. The TEM study showed that the transitions between the different phases follow topotactic mechanisms, through the formation of twinning boundaries, antiphase boundaries and planar defects. The annealed sample exhibits a mesomorph state and a reversible transition from this semi-ordered state to a crystalline phase. This dynamic transition takes place over a very wide temperature range from 620 to 1120 °C. The reversibility of the transition has been studied by DSC measurements. The crystallization energy of the orthorhombic phases is of the order of 10 J/g, at $T \approx 622$ °C as T decreases. The variation of the peak height observed as the annealing temperature increases is explained by the complex microstructures, which create an ill-defined energy barrier. Structural models related to the stuffed tridymite derivative structures are proposed for the new forms of the ferri-aluminate.

1. Introduction

Alkaline earth based aluminates and alumino-ferrites have been extensively studied because of their wide domains of applications as phosphors, luminous paints, ceramic pigments, membranes [1] and also because the tetracalcium aluminoferrite $Ca_4Fe_2Al_2O_{10}$ (or C4AF) is one of the five major components (10%) of Portland cement [2–3]. In this C4AF compound, which is the aristotype brownmillerite, there exists, regardless of symmetry changes, a continuous solid solution $Ca_2Al_{2-x}Fe_xO_5$ in the whole range $0 \leqslant x \leqslant 2$ [4–5], both Al^{3+} and Fe^{3+} cations occupying the tetrahedral and octahedral sites. Despite the close relationships between the brownmillerite and the derivative $LaSr_3(Fe_{1-x}Al_x)_3O_{9+\delta}$ phases [6], it was shown that, on the contrary, the solid solution is limited in the latter with the appearance of a second phase for $x > 0.25$. The stuffed tridymite derivatives AM_2O_4 (M = Si, Al, Fe, Ga, Li, Be, Mg, P…) form another class of interest, where the M cations are located in M_2O_7 units, which build rings of six corner sharing MO_4 tetrahedra and manage cavities for the large A cations (A = Na, Ca, Sr, Ba, Pb or NH_4…) [7]. These compounds show a complex polymorphism, as a function of the temperature and the cationic substitutions, which result in a simple lowering of the symmetry or real different topological arrangements.

The high temperature "HT" form of the tridymite is hexagonal (space group $P6_3/mmc$), with $a \approx 5.1$ Å $= A$, $c \approx 8.3$ Å $= C$ (A and C are commonly used as references for the parameters of the tridymite unit cell). In the alkaline earth based Ae^{2+}–(Al–Fe)–O systems (Ae = Ba, Sr and Ca), several "binary" oxides, aluminates or ferrites, are characterized by structures exhibiting close relationships with the tridymite. $SrAl_2O_4$, whose luminescent properties have been discovered 40 years ago [8], crystallizes in a monoclinic structure at room temperature (RT) [9] and undergoes a phase transition towards a hexagonal structure at 950 K [10]. The two forms of $SrAl_2O_4$, adopt the typical arrangement of the AlO_4 tetrahedra observed in the "HT" tridymite form, with an alternating orientation of the apical oxygens of the tetrahedra, namely "up" (U) and "down" (D), with regard to the basal plane of the rings formed by six corner sharing tetrahedra: the sequence is then UDUDUD. The mechanism of the phase transitions is still under discussion [9–13]. In spite of the existence of a metastable structure of $SrFe_2O_4$, which crystallizes in a stuffed tridymite structure with a sequence UDDDDD [14], no compound $SrFe_2O_4$ was reported in most of the phase diagrams $SrO–Fe_2O_3$ vs T. More recently a second structure has been evidenced with the sequence UUUDDD [15].

* Corresponding author. Fax: +33 231951600.
E-mail address: sylvie.malo@ensicaen.fr (S. Malo).

0022-4596/$ - see front matter © 2009 Elsevier Inc. All rights reserved.
doi:10.1016/j.jssc.2009.04.013

Because of the high temperature conditions required for the preparation of $SrAl_2O_4$ [16] and the stake in the properties, numerous technological solutions have been tested, especially the doping and substitution techniques, in order to stabilize derivative structures. A few studies have been reported on the substitution of Fe^{3+} for Al^{3+} in the stuffed tridymite and they all agree with the existence of only a tiny stability range of the mixed materials. Contrary to the perovskite system, the solid solution $CaAl_{2-x}Fe_xO_4$ is stabilised with a low iron content [17] and the investigation of the system $SrFeO_{3-\delta}$–$SrAl_2O_4$ [18–20] for the preparation of membrane reactors for natural gas conversion evidenced the formation of a dual-phase composite.

In the present paper, we report on the synthesis and characterisation of strontium alumino-ferrites $SrAl_{1.5}Fe_{0.5}O_4$, using powder X-ray diffraction (XRPD), transmission electron microscopy (TEM) techniques and thermal analyses. We evidence the existence of four iso-compositional phases. The monoclinic (denoted M-) and hexagonal (denoted H-) phases are isotypes of the pure aluminate $SrAl_2O_4$ whereas the two other ones, orthorhombic or pseudo-orthorhombic (denoted O_1- and O_2-) are original phases, characterized by a supercell.

2. Experimental

$SrAl_{1.5}Fe_{0.5}O_4$ compounds were synthesized by solid-state reaction using a two-steps process performed in air. Firstly, stoichiometric amounts of $SrCO_3$ and Fe_2O_3 were crushed in an agate mortar to obtain a homogeneous powder. The mixture was decarbonated in air at 900 °C for 12 h and then mixed with 0.75 mole of Al_2O_3. The as-synthesized sample was heated at 1350 °C for 24 h with a heating rate of 2 °C/min, slow cooled until 500 °C with a cooling rate of 20 °C/h and then, quenched down to room temperature. This sample is denoted A_{ss}.

Different treatments were applied to different parts of this as-synthesized sample, varying the heating temperatures between 800 and 1550 °C and the temperature decreasing modes, on the bases of different chemical and structural analyses. Two of these samples are detailed herein. The sample denoted A_{nn} was obtained by annealing the A_{ss} material at 800 °C in air; different heating plateaus ranging from 1 to 7 days as well as the cooling rate do not modify significantly the results. The sample denoted Q_{ch} was obtained by re-heating the A_{ss} sample at 1350 °C and quenching it in air. The nature of the precursors, thermal process and labels of the different samples are summarized in Table 1.

The XRPD data were collected at room temperature with a 'X' PERT Pro Philips diffractometer working with the Co$K\alpha$1 ($\lambda = 1.78901$ Å) in the range $3° \leqslant 2\theta \leqslant 120°$.

For the TEM study, a small piece of sample was crushed in an agate mortar containing ethanol and a droplet was deposited on a copper grid covered with holey carbon film. The cationic composition was determined using KEVEX energy dispersive spectroscopy (EDS) analyzers by averaging the cationic ratios of numerous crystallites; these measurements were coupled with the electron diffraction (ED) characterization. The electron diffraction investigation was carried out with a JEOL 200 CX equipped with a eucentric goniometer ($\pm 60°$). The reciprocal space was reconstructed by tilting around the crystallographic axes. The TEM study was carried out with a JEOL 2010F microscope (200 kV, Cs = 1 mm). The theoretical images were calculated with the MacTempas software for different focus and crystal thickness values. In the present images, the dark dots are related to the cations positions (the crystal thickness is of the order of 4.5 nm and the focus value close to −10 nm). The X-ray refinements were performed with the Fullprof Suite 1.00 (February 2007) software.

The thermogravimetric analyses (TGA) and differential scanning calorimetry (DSC) measurements were performed on a SDT 2960 TA Instruments, working in flowing air, N_2 and O_2

Table 1
Characteristics of the samples $SrAl_{1.5}Fe_{0.5}O_4$ (precursor and thermal process) and the stabilization of the different phases from ED and XRPD analyses.

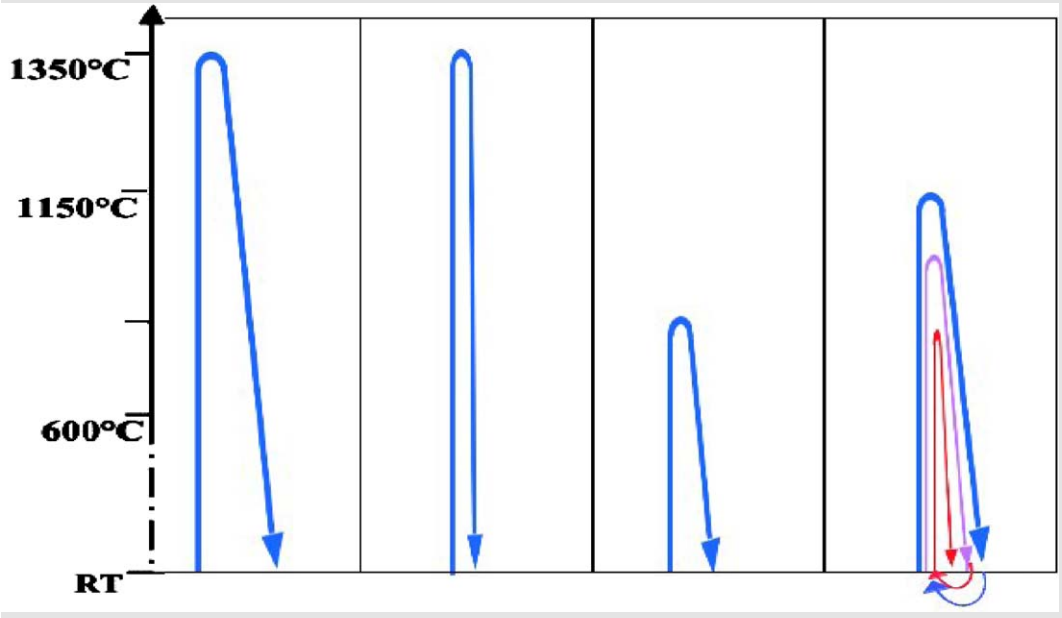

Precursor	Oxides	M	M	O_1+O_2
Sample label	A_{ss}	Q_{ch}	A_{nn}	DSC
Major phase	M	M	O_1+O_2	O_1/O_2
Minor phase	$(O_1/O_2)_w$	$(H)_m$	$(M)_w$	$(M)_{vw}$

atmospheres at a heating rate of 40 °C/min and a cooling rate of 10 °C/min. In a second step of experiments, the temperatures were changed between room temperature and different temperatures, denoted T_{MAX}, ranging between 850 and 1120 °C. Lastly, measurements were carried out by varying the heating and cooling rates (20, 10 and 5 °C/min) between RT and 1120 °C.

3. Results

The analyses of the samples were firstly carried out combining XRPD (Fig. 1), energy dispersive spectroscopy and electron diffraction data. The ED investigation showed that four phases related to the tridymite structure exist in more or less important

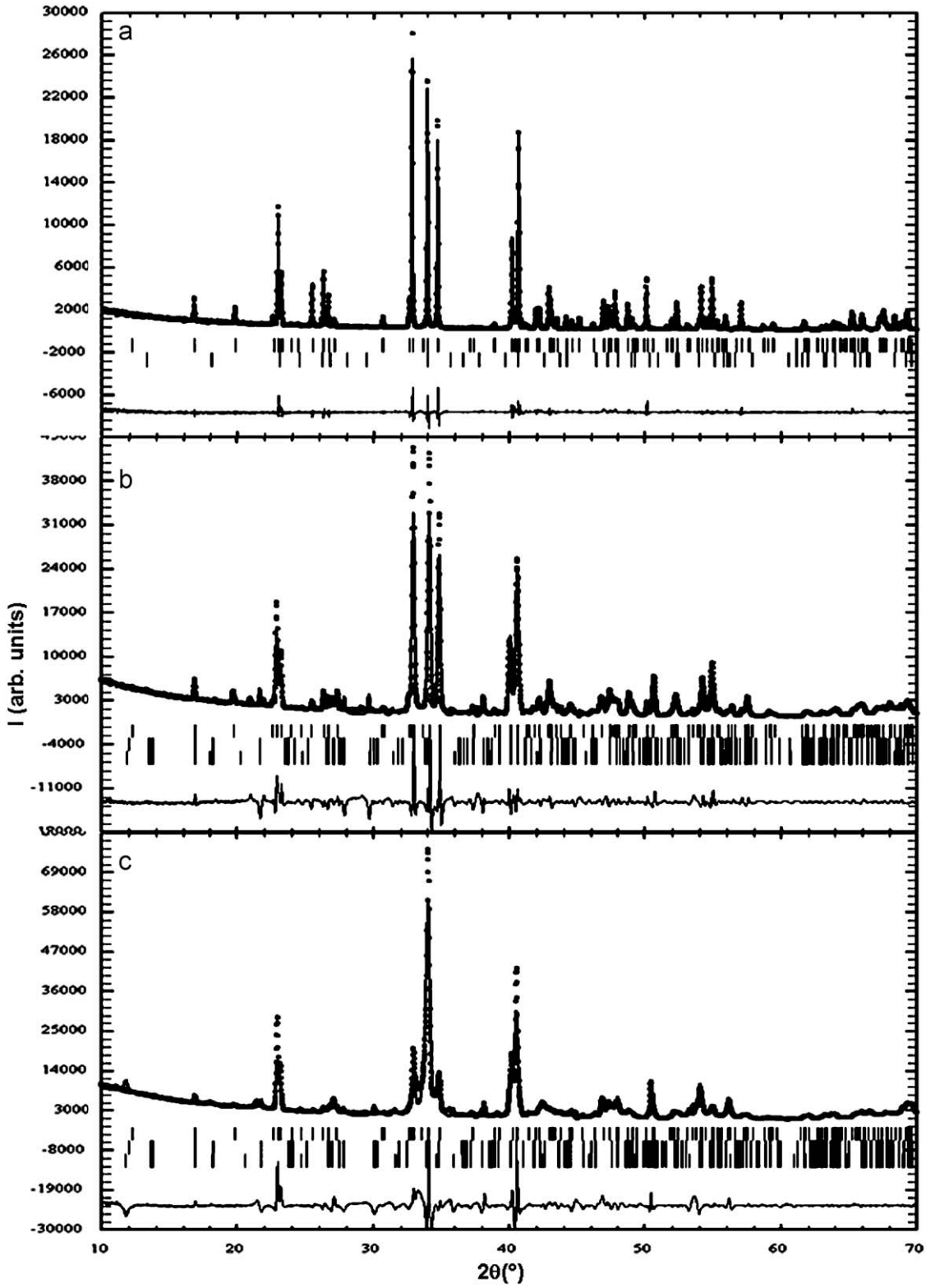

Fig. 1. Observed, calculated and difference XRD patterns of: (a) Q_{ch} quenched sample; $R_p = 7.07\%$, $R_{wp} = 9.12\%$, $R_{Bragg,M} = 5.01\%$, $R_{F,M} = 3.26\%$, $R_{Bragg,H} = 25.3\%$, $R_{F,H} = 10.2\%$. (b) A_{ss} as synthesized sample; $R_p = 10.8\%$, $R_{wp} = 17.4\%$, $R_{Bragg,M} = 5.56\%$, $R_{F,M} = 3.92\%$. (c) A_{nn} annealed sample; $R_p = 12.2\%$, $R_{wp} = 18.2\%$, $R_{Bragg,M} = 8.82\%$, $R_{F,M} = 3.51\%$.

Table 2
Lattice parameters of the parent $SrAl_2O_4$ structures (shaded) and $SrAl_{1.5}Fe_{0.5}O_4$.

	a (Å)	b (Å)	c (Å)		S.G.	Cell V (A^3)/tridymite unit cell	Ref.
$SrAl_2O_4$	**5.163**	**8.816**	**8.447**	**$\beta = 93°42$**	***P*2₁, *P*2₁/*m***	**383.8**	**[9]**
UDUDUD						**191.9**[b]	
$SrAl_2O_4$ (800 °C)	**8.926**	**8.926**	**8.49**	**$\gamma = 120°$**	***P*6₃**	**585.8**	**[10]**
						195.3[b]	**[18]**
$SrAl_2O_4$ (1000 °C)							
UDUDUD	**5.167**		**8.549**	**$\gamma = 120°$**	***P*6₃22**	**197.7**[b]	**[13]**
Extrapolated at RT	**5.13**		**8.44**	**$\gamma = 120°$**	***P*6₃22**	**192.4**[b]	**[11]**
M-$SrAl_{1.5}Fe_{0.5}O_4$	5.2157(1)	8.8857(1)	8.4669(1)	$\beta = 93°591(6)$	$P2_1$;$P2_1m$	391.6	[b]
						195.8[b]	
H-$SrAl_{1.5}Fe_{0.5}O_4$		8.939(1)	8.421(2)	$\gamma = 120°$	$P6_3$	582.7	[b]
						194.2[b]	
O_1-$SrAl_{1.5}Fe_{0.5}O_4$					$P2_1mn$		[b]
	15.454(2)[a]	8.957(1)[a]	8.443(1)[a]		$P11n$	1131.6	
O_2-$SrAl_{1.5}Fe_{0.5}O_4$					$P222_1$	194.7[b]	[b]

[a] Average values for the O_1- and O_2-structures.
[b] This work.

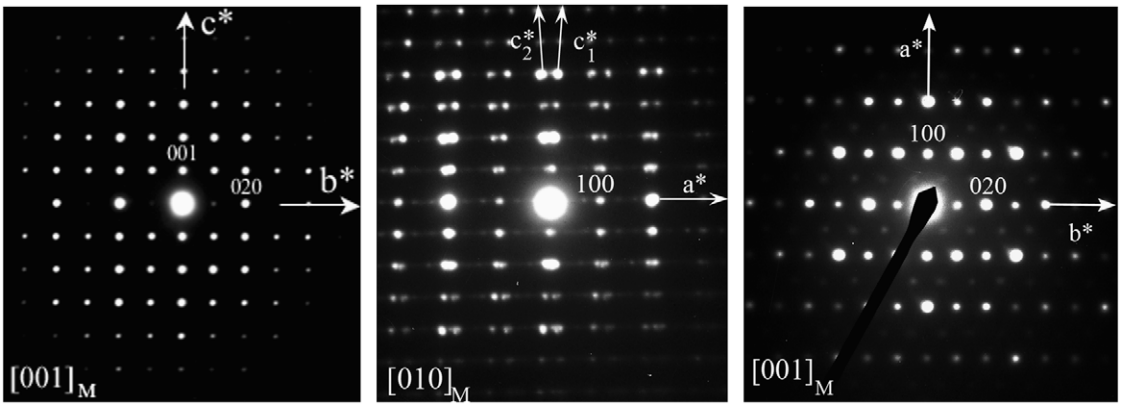

Fig. 2. (a) [100], (b) [010] and (c) [001] ED patterns of the M-$SrAl_{1.5}Fe_{0.5}O_4$.

proportions in each of the samples ($A_{ss}/A_{nn}/Q_{ch}$) detailed in the present work and the materials obtained in the run of the DSC measurements. Table 1 summarizes the main characteristics of these materials, as well as the major and minor phases stabilized in each of them.

3.1. EDS and thermal analyses

The EDS investigation confirmed that the actual Sr/Al/Fe ratio is 2/3/1, within the accuracy limits of the technique, with a standard deviation ± 0.07 for Sr and ± 0.05 for the metals in tetrahedral coordination (calculated per $SrAl_{1.5}Fe_{0.5}$ unit).

The TGA analyses of the A_{nn} sample have been carried out up to 1100 °C under air, N_2 and O_2 flow. The absence of weight variation, whatever the atmosphere, supports the stoichiometric formulation of AM_2O_4 oxometallate compounds. By decreasing *T*, a peak is observed on the three DSC curves at a temperature close to 623 °C, attesting that the material undergoes a phase transformation, independent of the atmosphere, especially of the oxygen pressure.

3.2. TEM study of the four forms: M-, H-, O_1- and O_2- $SrAl_{1.5}Fe_{0.5}O_4$ phases

In order to compare easily the different structures observed for the present $SrAl_{1.5}Fe_{0.5}O_4$ phases with the known stuffed tridymite structures, we have adopted the convention to keep the stacking direction of the rings as the *c* parameter, i.e. $C = c \approx 8.45$ Å and $b \approx \sqrt{3}A \approx 8.9$ Å, the common parameter to the four phases.

3.2.1. The monoclinic M-$SrAl_{1.5}Fe_{0.5}O_4$

The ED analyses of the Q_{ch} sample by the reconstruction of the reciprocal space evidenced that the majority phase has a monoclinic structure, denoted M-$SrAl_{1.5}Fe_{0.5}O_4$. The cell parameters, $a_M \approx A \approx 5.22$ Å, $b_M \approx \sqrt{3}A$, $c_M \approx C$ and $\beta \approx 93°$ (Table 2), suggest that the phase is isotypic with the monoclinic form of $SrAl_2O_4$ [9]. The [100], [010] and [001] basal ED patterns are given in Fig. 2. The only condition of reflection is $0\,k\,0$: $k = 2n$, consistent with $P12_11$ as possible space group (S.G.). Note that in Fig. 2c, the $0\,k\,0$: $k = 2n+1$ reflections are lighted by double diffraction phenomena while the splitting of the reflections in the [010] pattern (Fig. 2b) is characteristic of the presence of twinning domains, as a result of the monoclinic distortion.

3.2.2. Nanotwins in the M-$SrAl_{1.5}Fe_{0.5}O_4$

An example of $[010]_M$ HREM image with twinning domains generated by the monoclinic distortion (β close to 93°) is given in Fig. 3a. The twin boundaries (TB) are parallel to $(100)_M$ and the average width of the domains is a few ten nanometers. In such an interface, the Sr atoms and tetrahedral layers are not modified as illustrated in the [010] projected structure of two oriented domains of Fig. 3b (the larger blue circles represent the Sr positions and the medium red ones within the polyhedra the Al/Fe positions. Another origin of the twinning phenomena is associated

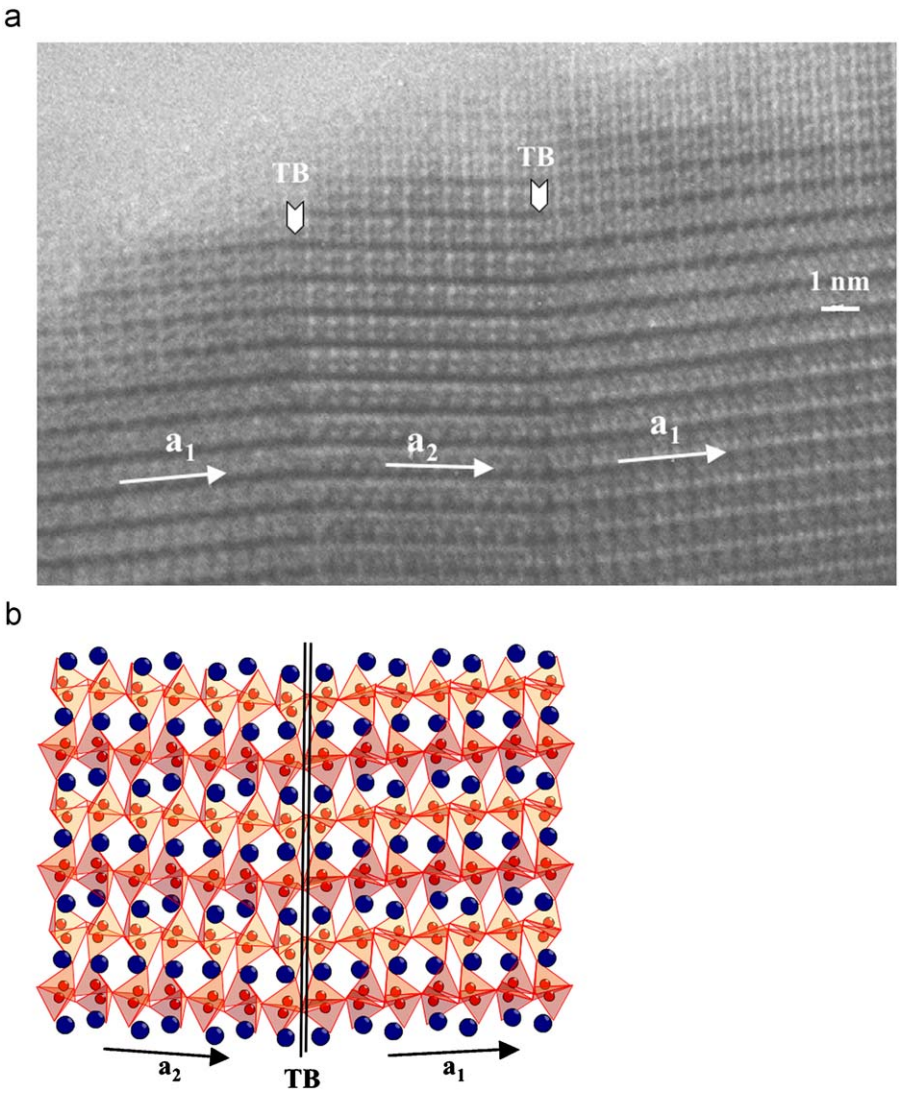

Fig. 3. M-$SrAl_{1.5}Fe_{0.5}O_4$: (a) [010] HR image of the twin domains. The twin boundaries (TB) are parallel to (100); (b) [010] projected twinned domains and boundary.

with the lowering of the symmetry from hexagonal to monoclinic and easily observed by viewing the crystallites along the $[001]_M$ direction. The experimental pseudo-hexagonal $[001]_M$ pattern given in Fig. 4b arises from the overlap of three variants since the intense reflections, $2\,0\,0_M$, $1\,3\,0_M$ and $1\,\bar{3}\,0_M$ (Fig. 2c) form a pseudo-hexagonal system (note that the two circled reflections along $\vec{a}_1^*$ result from double diffraction); the different systems are schematically drawn besides the $[001]_M$ pattern. The corresponding HREM $[001]_M$ images show the formation of small domains rotated by 120°, as illustrated in Fig. 4a. The patchwork-like appearance of the images comes from the small size of the twin domains. The coherent twin boundaries are parallel to the $(010)_M$ and $(010)_H$ of the $P6_3$ hexagonal planes containing the Sr atoms and the oxygens atoms; two variants and their interface are schematically drawn in Fig. 4c. Moreover, one also observes the presence of one type of additional planar defects (PD) parallel to (100). The nature of these defects, premises of the orthorhombic superstructures, will be discussed further.

3.2.3. *The hexagonal H-$SrAl_{1.5}Fe_{0.5}O_4$*

In the pure aluminate phase, the ideal undistorted structure of the high temperature form ("HT" tridymite) corresponds to $a \approx 5.5\,\text{Å} = A$, $c \approx 8.4\,\text{Å} = C$ and space group $P6_322$ [11–13]. The mechanism transition between the RT monoclinic $P2_1$ and the HT $P6_3$ structures has been the subject of controversy, with different intermediate phases proposed from XR and neutrons diffraction refinements at temperatures ranging between 650 and 800 °C [13]. According to the relationships between the different phases of the system, the actual presence of the hexagonal phase at RT (and its unambiguous identification in a sample) was confirmed by tilting around the $\vec{c}^*$ (common axis to the different structures). The ED study evidenced that H-$SrAl_{1.5}Fe_{0.5}O_4$ is the minority phase in the Q_{ch} sample and the EDS analyses, carried out on each of the characterized grains, showed that the cationic ratio is Sr/Al/Fe ≈ 2/3/1, i.e. does not show any significant difference with the results obtained for the grains exhibiting the M-$SrAl_{1.5}Fe_{0.5}O_4$ structure. The reconstruction of the reciprocal space cell leads to $a_H \approx 8.98\,\text{Å}$ and $c_H \approx 8.30\,\text{Å}$ and the condition of reflection consistent with the $P6_3$ space group. The cell parameters and space group of the H-$SrAl_{1.5}Fe_{0.5}O_4$ phase suggest that it is isotype of the hexagonal form of $SrAl_2O_4$ observed in the course of the transition between the monoclinic and HT $P6_322$ form [10]. The $[001]_H$ and $[110]_H$ ED patterns are given in Fig. 5. Compared to the hexagonal forms of the pure aluminate, which have been previously studied at high temperature, the presence of this phase at ambient in the A_{ss} and Q_{ch} samples could be imputed to two concomitant mechanisms. The first one deals with the

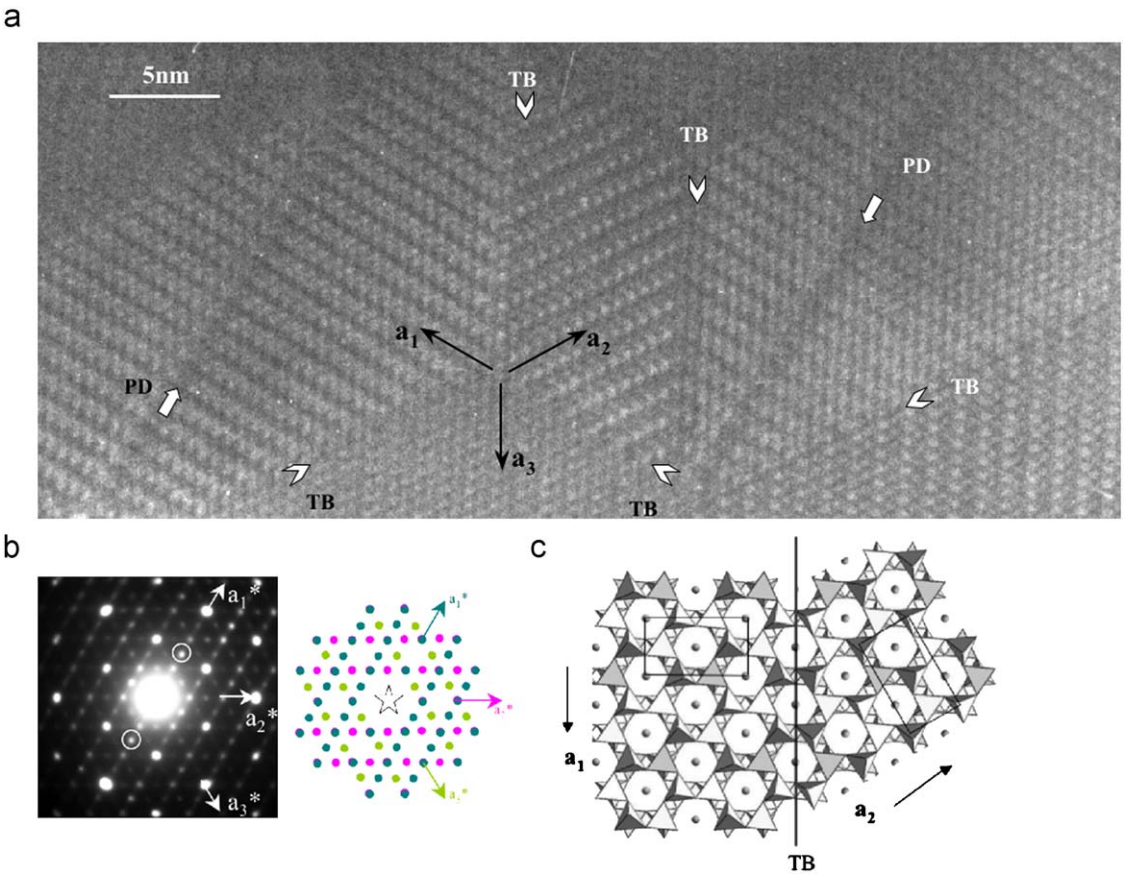

Fig. 4. (a) [001] image showing the 120° oriented domains and planar defects (PD) perpendicular to the twin boundaries (TB); (b) experimental [001] ED pattern and schematic representation of the three variants; (c) representation of two variants through the TB.

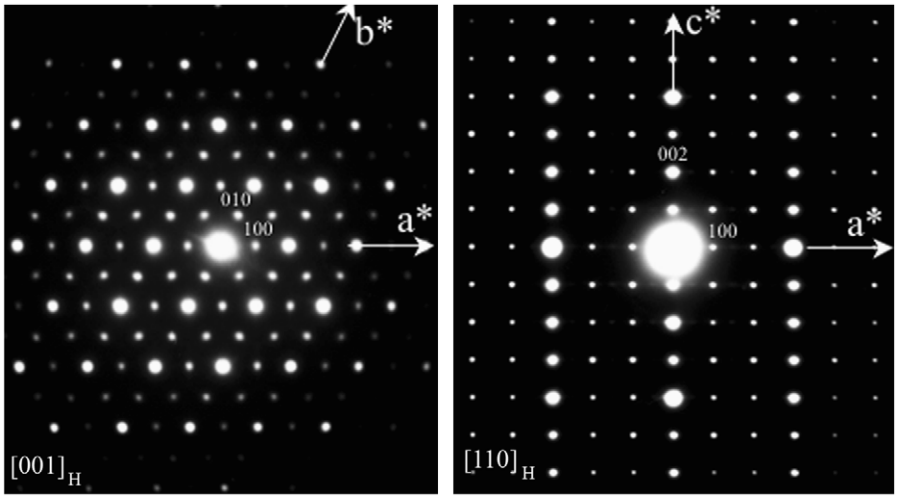

Fig. 5. [001] and [110] ED patterns of H-$SrAl_{1.5}Fe_{0.5}O_4$ phase (the 0 0 l, $l = 2n+1$ reflections appear from double diffraction phenomena).

introduction of iron in the matrix and the second with its trapping in the monoclinic framework under mechanical strains during the cooling process.

3.2.4. *The two O_1- and O_2-$SrAl_{1.5}Fe_{0.5}O_4$*

The existence of two original phases was detected in the A_{ss} sample; they have been stabilized as the major phases in the A_{nn} sample (Table 1). The reconstruction of the reciprocal space, carried out on numerous crystallites, showed that the two phases systematically coexist. They are characterized by common parameters, $a \approx 15.4$ Å, $b \approx 9.0$ Å, $c \approx 8.4$ Å and $\beta \approx 90°$, and denoted O_1- and O_2-$SrAl_{1.5}Fe_{0.5}O_4$. The two phases are metrically similar but differ by their space groups (Table 2).

The condition of reflection $h\,k\,0$: $h+k = 2n$ for the O_1-$SrAl_{1.5}Fe_{0.5}O_4$ phase is observed, which involves $P2_1mn$ and $Pmmn$ as

possible space groups considering an orthorhombic symmetry. However, the presence of numerous nanodomains and planar defects hinders to go further in the determination of the presence of certain symmetry elements by ED techniques so that a lowering of the symmetry ($\beta \approx 90^\circ$) cannot be definitively rejected and the space group $P11n$ must also be retained. One can note that there exist close relationships between these parameters and those of $CaAl_2O_4$ [21], as discussed further.

For the O_2-$SrAl_{1.5}Fe_{0.5}O_4$ phase, the condition of reflection is $0\,0\,l$: $l = 2n$, which involves the space groups $P222_1$ for an orthorhombic cell and $P112_1$ or $P112_1/m$, accounting the same limitations as above on the accurate determination of the symmetry element by ED techniques. The two common ED patterns, $[010]_O$ and $[100]_O$, are given in Fig. 6a and b; the different $[001]_{O1}$ and $[001]_{O2}$ ED patterns recorded by tilting around $\vec{a}^*_O$ are compared in Fig. 6c and d.

The ED and TEM studies of the A_{nn} sample show that the O_1- and O_2-$SrAl_{1.5}Fe_{0.5}O_4$ phases are observed either in the form of tiny grains or, for the greater part, coexist in the form of parallel domains within the grains, as illustrated in Fig. 7. The domains O_1- and O_2- exhibit a common $\vec{b}_{1,2}$ axis, with coherent (100) twin boundaries. The positions of the cation columns are projected as the darker zones, and the [001] images of O_1-$SrAl_{1.5}Fe_{0.5}O_4$ phase are characterized by a centred contrast of bright dots while those of the O_2-$SrAl_{1.5}Fe_{0.5}O_4$ phase are characterized by the alternation along [100] of a double row of bright dots alternating with one row of grey dots. All the simulated images in insert have been calculated from hypothetical models discussed in the section devoted to the structural mechanisms.

As a first conclusion, taking the unit cell of the tridymite structure ($Z = 1$) observed at high temperature for the parent structure $SrAl_2O_4$ as reference, the three cells are drawn in Fig. 8 and the metrical relationships between the cell parameters are the following:

- H-$SrAl_{1.5}Fe_{0.5}O_4 = \sqrt{3}A \times \sqrt{3}A \times C$; $P6_3$ $Z = 3$
- M-$SrAl_{1.5}Fe_{0.5}O_4 = A \times \sqrt{3}A \times C$ and $\beta \approx 93^\circ$; $P2_1$ $Z = 2$
- O_1-$SrAl_{1.5}$ $Fe_{0.5}O_4 = 3A \times \sqrt{3}A \times C$; $P2_1mn$, $Pmmn$ or $P11n$ $Z = 6$
- O_2-$SrAl_{1.5}Fe_{0.5}O_4 = 3A \times \sqrt{3}A \times C$; $P222_1$ or $P112_1$, $P112_1/m$ $Z = 6$

3.3. XRD analyses

The XRPD pattern of the Q_{ch} sample (Fig. 1a) is very close to the one reported for the monoclinic $SrAl_2O_4$ (10) and only the ED investigation has allowed to detect the presence of the hexagonal form. In the XRPD pattern of the A_{ss} sample (Fig. 1b), the presence of the monoclinic phase is still visible but, for example, the intensity of the group of reflections around $2\theta = [25^\circ–28^\circ]$ is significantly decreased while additional reflections are observed. In the XRPD pattern of the A_{nn} sample (Fig. 1c), the characteristic peaks of the monoclinic phase are scarcely visible.

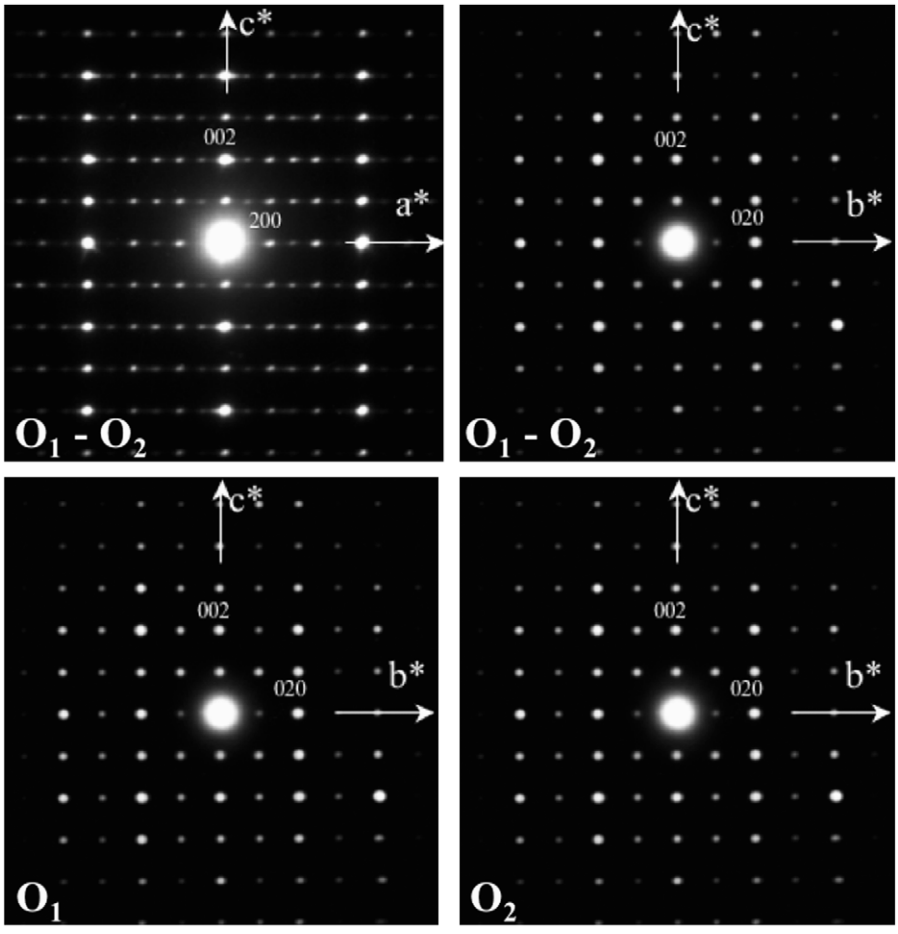

Fig. 6. (a) [010] and (b) [100] ED patterns of the O_1- and O_2-$SrAl_{1.5}Fe_{0.5}O_4$ phases (note that the [001] ED patterns differ by the condition $0\,0\,l$ but the $l = 2+1$ reflections of the O_2-phase result from double diffraction phenomena); (c) [001] ED patterns of the O_1- and (d) [001] ED patterns of the O_2-phases.

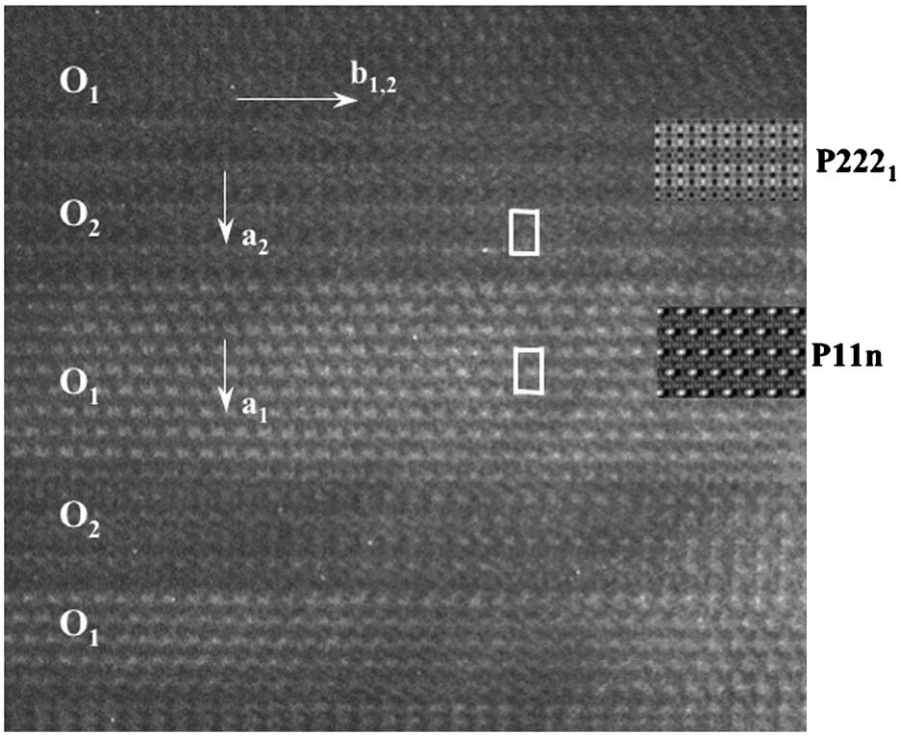

Fig. 7. [001] HR image showing the coexistence of the O_1- and O_2-$SrAl_{1.5}Fe_{0.5}O_4$ phases in the form of nanometric thick lamella, stacked along $\vec{a}$. The simulated images have been calculated from the positions determined for the "ideal" models given in Fig. 14.

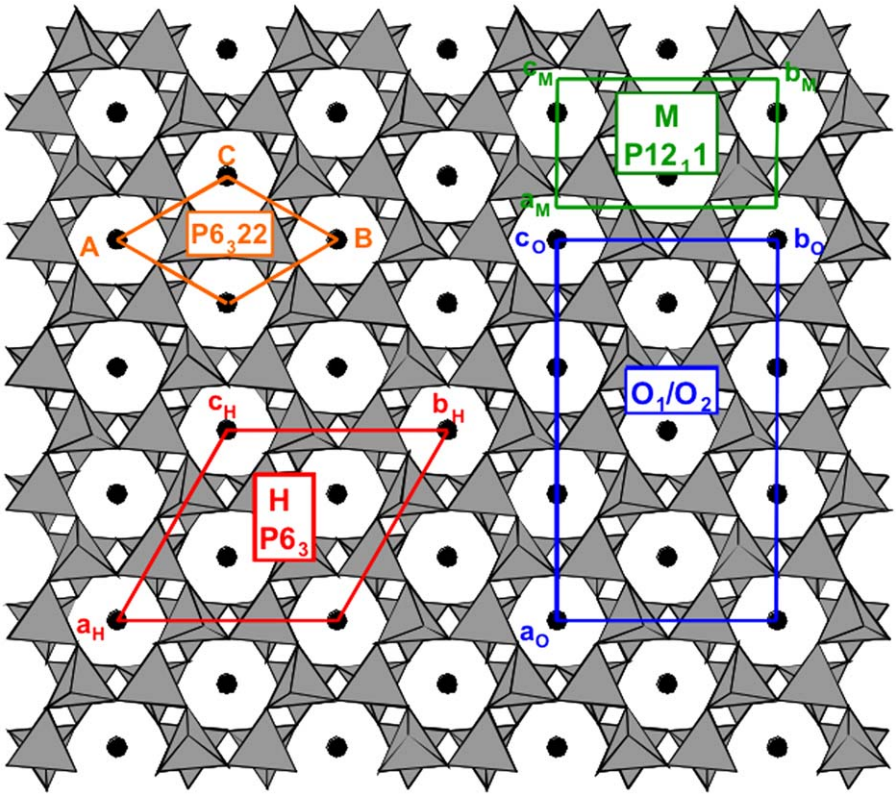

Fig. 8. [001] projection, in the direct space, of the different cells of the H-($P6_3$), M-($P2_1$), O_1- and O_2-$SrAl_{1.5}Fe_{0.5}O_4$ phases.

3.3.1. *Rietveld refinements details*

Structural refinements of M- and H-$SrAl_{1.5}Fe_{0.5}O_4$ phases have been carried out simultaneously on the XRPD pattern of the Q_{ch} sample, in agreement with the ED results. The cell parameters and the atomic coordinates were refined using the structures of the monoclinic [9] and hexagonal [10] forms of $SrAl_2O_4$ as starting

models and supposing that the Al sites are occupied at 75% by Al atoms and at 25% by Fe atoms. In order to describe the M-$SrAl_{1.5}Fe_{0.5}O_4$ phase in a $A \times \sqrt{3}A \times C$ cell, its initial crystal structure was deduced from the monoclinic $SrAl_2O_4$ structure transform by a (c, −b, a) cell permutation. The Al/Fe–O distances within the tetrahedra have been constrained between 1.6 and 1.9 Å. The refinement of cell parameters, profile parameters, atomic coordinates, thermal factors (one B thermal factor has been refined per atom type found in both phases) and background parameters leads to the global agreement factors, $R_p = 7.01\%$, $R_{wp} = 9.07\%$ and $\chi^2 = 4.74\%$ and to the structures factors, $R_{Bragg} = 5.05\%$ and $R_F = 3.24\%$ for the monoclinic phase and to $R_{Bragg} = 25.9\%$ and $R_F = 11\%$ for the hexagonal phase. The observed, calculated and difference X-ray powder patterns of the sample are given in Fig. 1a, the atomic coordinates of the monoclinic phase are reported in Table 3. The detailed refinement parameters of Q_{ch} sample and inter-atomic distances of the monoclinic phase are reported in supplementary Q_{ch}.cif file and Tables 1S and 2S, respectively. These files can be found in the online version. Note that, for the hexagonal phase, only the cell parameters are reported in the tables; its atomic coordinates could not be determined precisely because of its weak ratio and the small size of its domains. These phenomena are likely responsible for the poor agreement factors.

For the study of orthorhombic phases, the simplifying hypothesis of a single set of parameters (deduced from the TEM study) has been put forward. The XRPD data of the A_{ss} and A_{nn} samples have been considered for the refinement of the cell and profile parameters. The refinements have been performed by using the crystal structure of the monoclinic $SrAl_{1.5}Fe_{0.5}O_4$ phase and the cell parameters of O_1/O_2-phases. A set of averaged parameters has been obtained, ($a = 15.454(3)$ Å, $b = 8.957(2)$ Å, $c = 8.443(2)$ Å). The observed, calculated and difference XRPD patterns of A_{ss} and A_{nn} samples are reported in Fig. 1b and 1c respectively. The close structural relationships between the coexistent monoclinic and orthorhombic phases, the nanoscale domains and complex order–disorder phenomena increase the difficulty to refine the XRPD patterns and to go further in the structures refinement. Especially, hypothetical models proposed for O_1 and O_2 in the discussion section could not be confirmed by XRPD of A_{ss} and A_{nn} samples.

3.3.2. Structural comments

The cell parameters of M-$SrAl_{1.5}Fe_{0.5}O_4$ phase are longer than the ones of the isotypic $SrAl_2O_4$ phase (Table 2), in agreement with the larger ionic radius of Fe^{3+} ions ($r^{IV}_{Fe} = 0.49$ Å against $r^{IV}_{Al} = 0.39$ Å). For the hexagonal phase, our H-$SrAl_{1.5}Fe_{0.5}O_4$ phase is stabilised at RT and, moreover, mainly trapped in the monoclinic matrix so that a direct comparison can be hardly carried out since the previous reported data for $SrAl_2O_4$ have been recorded at high temperature (or extrapolated). Similarly the Al/Fe–O distances observed in the monoclinic $SrAl_{1.5}Fe_{0.5}O_4$ phase are larger than the ones observed in the aluminate isotype (supplementary material, Table 2S), but the Sr–O distances are equivalent in both isotypes. Note that the mean $d_{Al/Fe-O}$ distances are equivalent (ranging between 1.76(1) and 1.80(2)Å) for the four crystallographically independent tetrahedra; as no signature of ordering is detected, the refinement of an Al/Fe ordering has not been attempted.

Table 3
Atomic parameters for M-$SrAl_{1.5}Fe_{0.5}O_4$.

Atom	Site	x	y	z	B^*_{iso} (Å^2)	Occupancy
Sr(1)	2a	0.2499(4)	0.00000	0.4912(2)	1.15(3)	1.0
Sr(2)	2a	0.2031(3)	0.0066(3)	0.0316(2)	1.15(3)	1.0
Al(1)/Fe(1)	2a	0.711(1)	0.1689(9)	0.1916(8)	2.04(6)	0.75/0.25
Al(2)/Fe(2)	2a	0.732(1)	0.1630(7)	0.7970(8)	2.04(6)	0.75/0.25
Al(3)/Fe(3)	2a	0.226(1)	0.3326(8)	0.7092(8)	2.04(6)	0.75/0.25
Al(4)/Fe(4)	2a	0.801(1)	0.8300(8)	0.6814(8)	2.04(6)	0.75/0.25
O(1)	2a	0.430(2)	0.829(2)	0.265(1)	1.42(9)	1.0
O(2)	2a	0.592(2)	0.683(2)	0.731(1)	1.42(9)	1.0
O(3)	2a	0.351(2)	0.518(2)	0.329(1)	1.42(9)	1.0
O(4)	2a	0.904(2)	0.022(2)	0.271(1)	1.42(9)	1.0
O(5)	2a	0.933(2)	0.705(1)	0.167(1)	1.42(9)	1.0
O(6)	2a	0.895(2)	0.348(1)	0.209(1)	1.42(9)	1.0
O(7)	2a	0.888(2)	0.776(1)	0.489(1)	1.42(9)	1.0
O(8)	2a	0.653(2)	0.119(1)	0.990(1)	1.42(9)	1.0

4. TEM observation of the phase transitions

The TEM study of the A_{ss} sample evidenced that the O_1- and O_2- phases arise in the hexagonal and monoclinic matrices through complex transformation mechanisms. The different steps of this evolution are illustrated by several ED patterns and TEM images.

4.1. ED study

In the [010] ED patterns, the intense reflections $2\,0\,0_M$ and $3\,0\,0_H$ of the M- and H- phases (Fig. 9a—pattern 1) correspond to the same inter reticular distance (basic spots of the tridymite unit cell). During the transformation, the two phases coexist within the same grain so that, along [100]*, weaker spots appear in between the $1\,0\,0_M$ and $1\,0\,0_H$ (Fig. 9a—pattern 2), superposed and elongated as the result of more or less extended domains of each phase. The formation of diffuse nodes and streaks results of the smallness of these domains intergrown in a disordered manner (Fig. 9a—pattern 3). In the last steps, intermediate spots are observed in incommensurate (Fig. 9a—pattern 4) or commensurate positions (Fig. 9a—pattern 5) attesting of the stabilization of local modulated structures. In the pattern 5, five intermediate spots (two intense and three weak satellites) are observed up to their equal intensity (Fig. 9a—pattern 6), attesting of the stabilization of the superstructure with a tripling of the a_M parameter, i.e. 3*A*.

The very intense reflections of the [001] ED patterns of the A_{ss} sample fit with the system of the high temperature form of a $P6_322$ structure (orange spots in Fig. 9b—patterns 1 and 2) and the other systems of reflections attest of the superposition of the H- (red spots) and M-types (green spots) phases. The difference in intensity of one or the other system depends on the majority phase present in the selected area. In the A_{nn} sample, besides the grains characteristic of the presence of single O_1- or O_2-domains, most of the ED patterns are characterised by the aforementioned twinning phenomena (Fig. 9b—patterns 3 and 4). Some of them present also diffuse scattering phenomena, which result in diffuse intensity rows along the basic axes of the different structures (supplementary material, Fig. 1S) and attest of the existence of numerous defects along these axes.

4.2. HREM study

The study of the planar defects detected in the M-$SrAl_{1.5}Fe_{0.5}O_4$ phase evidenced the close relationships between the formation of these PD, which are generally three times the a_M periodicity wide, i.e. ≈15.4 Å, and their increasing density up to the stabilisation of one of the O_1- and O_2-phases. A first example is given in the [010] image of Fig. 10, with three planar defects (indicated by white arrows) in the M-matrix; the PD are parallel to

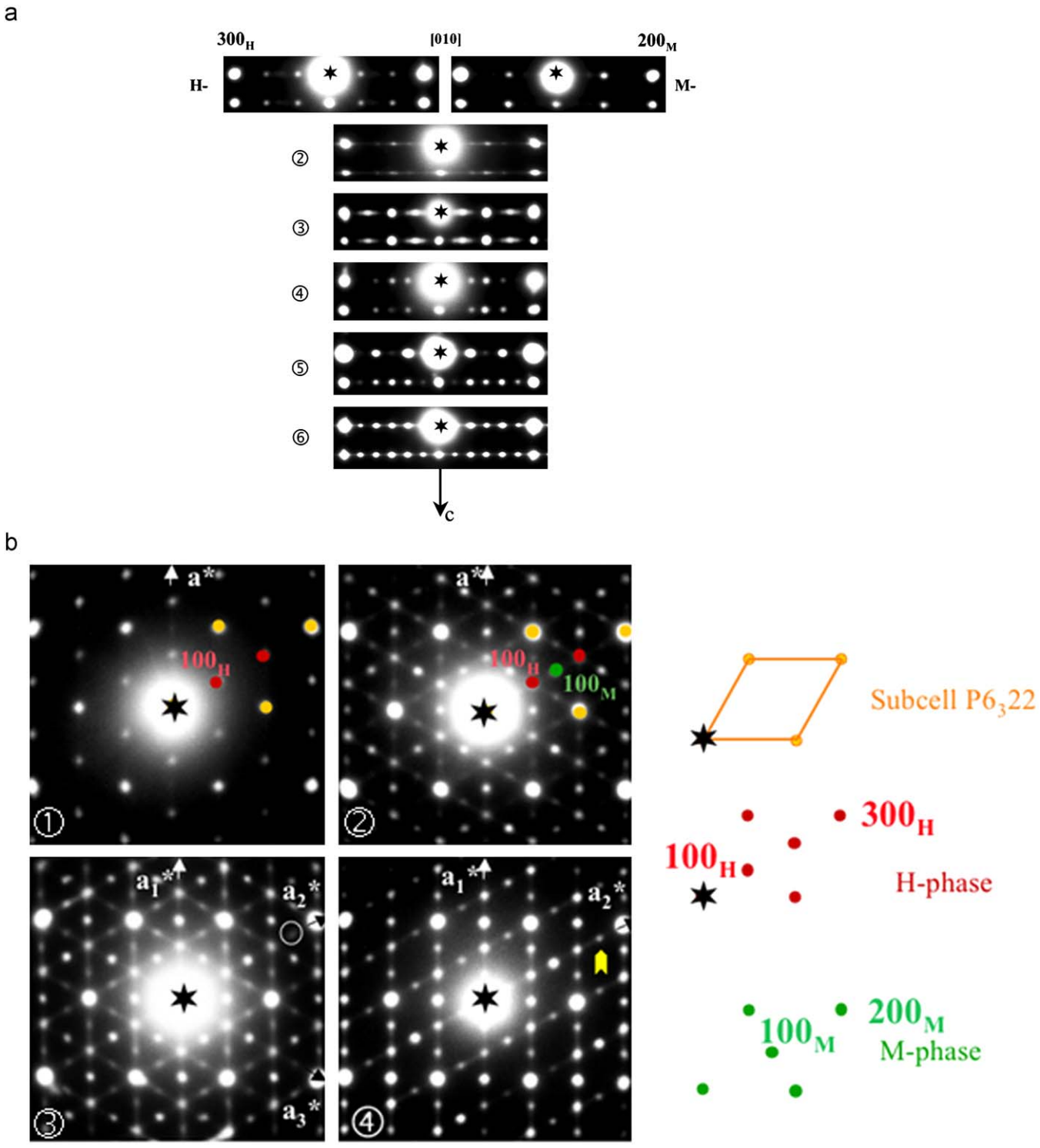

Fig. 9. Transformation mechanism viewing: (a) six [010] ED patterns starting from the H- and M-parent structures. (b): four [001] ED patterns, the theoretical patterns of the parent structures are drawn to show the intense nodes.

$(100)_M$, as the twin boundary (TB_M) between two monoclinic domains and the interface (represented by a double line) between the M- and O-domains. Viewing these $(100)_M$ planar defects along [001], the contrast of the defective slice is characterized by the formation of three rows of staggered brighter dots (see white arrow "PD"), parallel to $\vec{b}$, surrounded by rows of less bright dots Fig. 11a. They form sheets, 15.4 Å wide along $\vec{a}$, which are the premises of the centred contrast of O_1-$SrAl_{1.5}Fe_{0.5}O_4$. The transition between the M- and O_2-$SrAl_{1.5}Fe_{0.5}O_4$ phases is illustrated in Fig. 11b: one observes the local disturbance of the contrast in the M-matrix over two or three a_M units (the small double arrows correspond to about 10.3 Å, i.e. 2*A*); the defective zones are the premises of the striped contrast of O_2-$SrAl_{1.5}Fe_{0.5}O_4$.

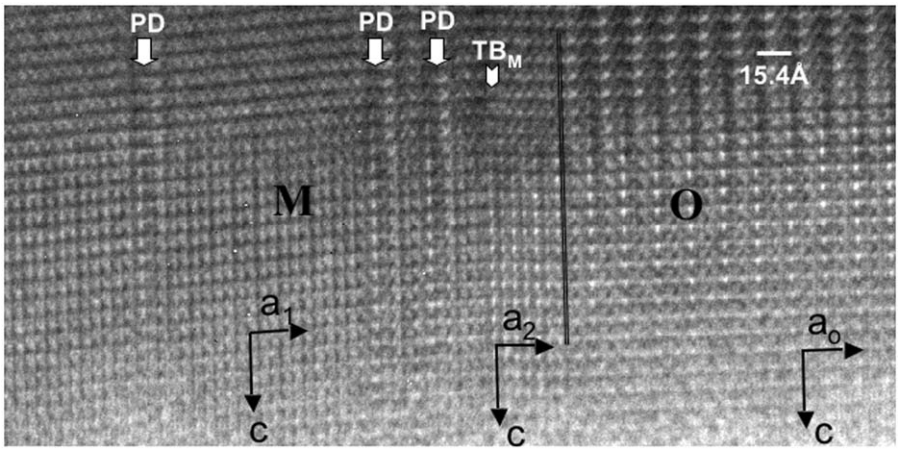

Fig. 10. [010] HREM image showing the coexistence of the two monoclinic domains (left part) and orthorhombic (right part) structures. The interface between the M- and O-$SrAl_{1.5}Fe_{0.5}O_4$ structures is indicated by a black double-line. In the first M-domain, three (100) planar defects (PD) are observed.

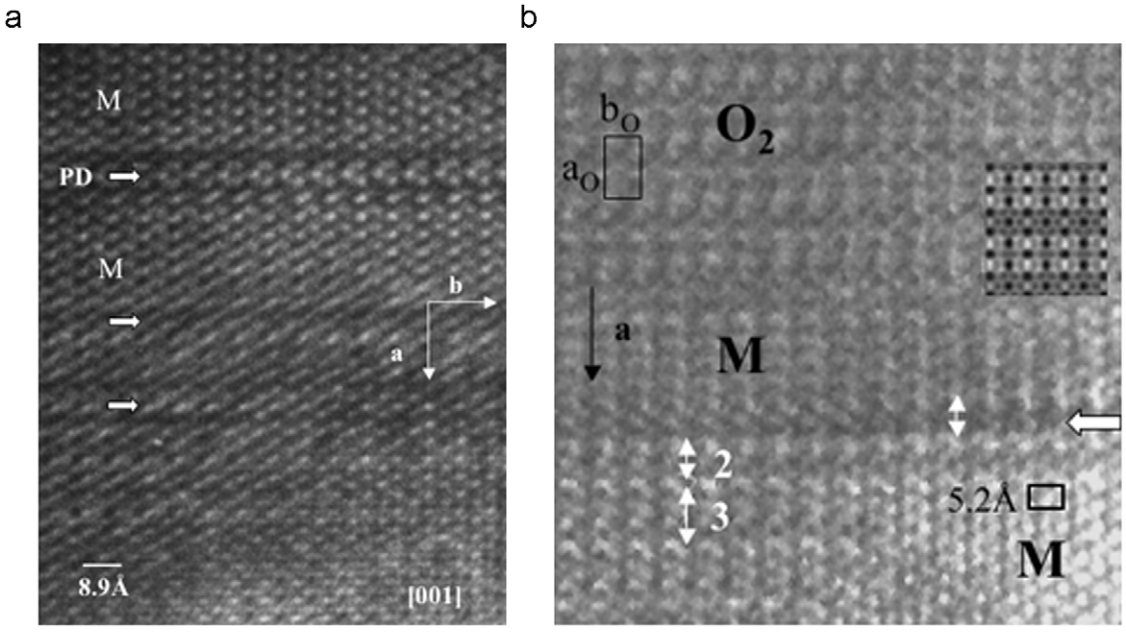

Figure 11. (a) [001] image of one M-$SrAl_{1.5}Fe_{0.5}O_4$ in which the density of (100) planar defects is relatively high. (b) [001] image of the transition between the M- and O_2-phases (two UDUDUD structures).

As evidenced by the ED study, the formation of planar defects along another direction makes more complex the mutual arrangement of the different phases. This is illustrated in Fig. 12, through another example. The $[001]_M$ ED pattern (not shown herein) is characterized by two M-$SrAl_{1.5}Fe_{0.5}O_4$ variants, similarly to Fig. 9b–pattern 4; they differ by the existence of elongated additional nodes along $[010]^*_M$ instead of $[100]^*_M$. These extra nodes are generated by disorder phenomena, which occur along $\vec{b}_M$ instead of $\vec{a}_M$ in the above examples. The lattice images evidence the local formation of (010) defective slices characterized by short-range ordering phenomena associated with a periodicity, which is two times and three times the b_M parameter (note that the $\times 3b_M$ periodicity could be interpreted as a polytype $[2b_M+b_M]$), as exemplified in Fig. 12, and also the easy formation of superdislocation (Fig. 2S in supplementary material).

5. Thermal process of the reaction

The differential scanning calorimetry measurements have been carried out on the same piece (at constant weight) of the A_{nn} sample following different cycles as we used in the synthesis process (Table 1). The temperature was increased, up to a maximum ranging between $T_{MAX} = 1120$ and 830 °C, and then decreased. All the curves (results summarized in Fig. 13) exhibit a single peak at a temperature T_{peak}, ranging between 620 and 630 °C, except the curve obtained for $T_{MAX} = 830$ °C for which the peak is scarcely detectable. The height of the peaks decreases as T_{MAX}; it is important to specify that the experiments have not been carried out following the order of decreasing T_{MAX} and that they are reproducible, i.e. independent of the cycle sequence. These results confirm that the transition temperature is close to 620 °C, and several points are of interest.

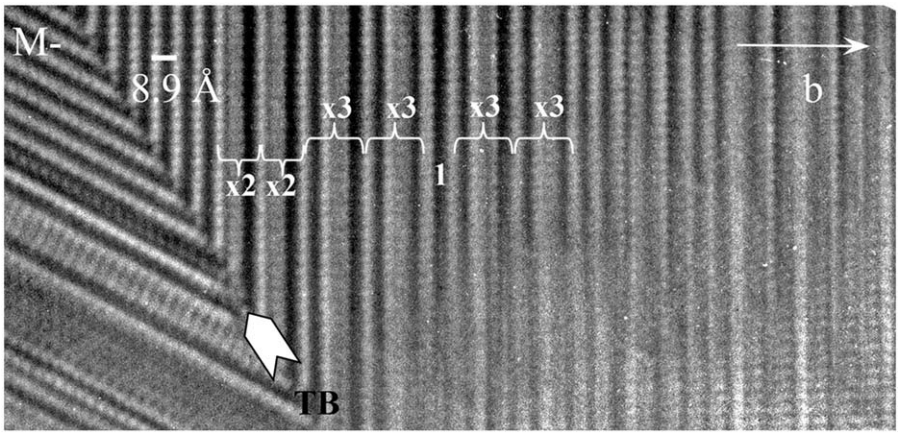

Fig. 12. [001] Image of one M-$SrAl_{1.5}Fe_{0.5}O_4$ showing existence of ordering phenomena along $\vec{b}$ leading to multiple periodicities of the b parameter.

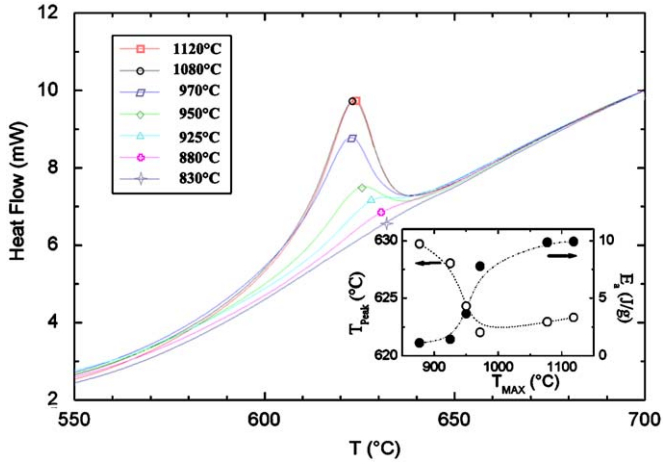

Fig. 13. DSC curves obtained by decreasing T (insert: peak height E_a and T_{peak} as a function of T_{MAX}).

The fact that there is only one peak, by decreasing T, suggests that there is a single "transformation" mechanism HT→LT rather uniform.

The fact that the intensity of the peak of $SrAl_{1.5}Fe_{0.5}O_4$ varies with T_{MAX} implies that it cannot be directly correlated to an enthalpy of the transition but that it is dependant of a fraction of the sample, fraction that is necessarily dependant of T_{MAX}. Similar effects have been observed in NiTi film for which the DSC peak height increases as the annealing temperature increases [22], the multiple phase transformations via an intermediate phase or direct martensitic/austenite transformation being studied by DSC and TEM. Another example has been reported for the structural changes of the gallium orthophosphate under thermal treatments, followed by XRPD and thermo-analytical methods [23].

The maximum of peak height, which is observed for $T_{MAX} = 1120\,^{\circ}C$, is of the order of 10 J/g. This value is consistent with that reported for the reversible transition between the high and low temperature forms of the pure strontium aluminate $SrAl_2O_4$ (10), 2.3 cal/g (9.628 J/g) and comparable with those observed for the tridymite. Another comparison is of interest, that of the barium-based aluminate $BaAl_2O_4$, which is often compared to $SrAl_2O_4$ since it exhibits a similar HT form [24] with $A \times A \times C$ parameters and the $P6_322$ space group. The room temperature form of $BaAl_2O_4$ presents the same UDUDUD arrangement of the tetrahedra as $SrAl_2O_4$ but differs by its symmetry and cell parameters ($2A \times 2A \times C$ and space group $P6_3$). Another remarkable difference is the absence of thermal signal in $BaAl_2O_4$ at the phase transition and in the thermal runs up to 1000 °C [25]. However, this transition (paraelectric (PE)–ferroelectric (FE)) has been studied *in situ* by transmission electron microscopy as a function of T [26]. It was shown that the reversible transition takes place over a wide range of temperature, ranging between 130 and 400 °C. The authors evidenced the formation of different orientation variants, function of the symmetry of the high and low temperature forms, and different types of antiphase boundaries (AB). This TEM study suggests that the activation energy is of the same order that the one observed in our case (a few J per g) but that the sensitivity of the thermo-analytic device could not be sufficient to detect this second order transition.

In the present sample, the dependence of the peak height with T_{MAX} can be associated with the fraction of the phase which suffers the transition at 620–630 °C. As the initial and final states are in majority the orthorhombic phases, this suggests that the fraction of the phases needs to reach 1120 °C to be entirely transformed in the high T form. The orthorhombic structures are partially retained as long as the sample has not seen temperatures higher than 1120 °C. Note that no peak has been observed on heating runs, up to 1120 °C despite the exothermic peaks appear on cooling. This behaviour is similar to that reported for the gallium orthophosphate [23,27]. We can conclude that in the present $SrAl_{1.5}Fe_{0.5}O_4$ material, the complete transition LT→HT (from the mesomorph state at LT towards the single phase form at HT) has a high barrier, likely associated to the arrangement of the complex variants, so that the transition temperature is not well defined. On the opposite, the reverse transition HT→LT from the single phase towards the mesomorph state occurs around 620–630 °C.

The measurements carried out by varying the cooling rate from $T_{MAX} = 1120\,^{\circ}C$ (20, 10 and 5 °C/min) do not evidence significant effects: the peaks do not suffer any significant translation in temperature ($T_{peak} = 623\,^{\circ}C$) and the crystallization energy remains unchanged (of the order of 10 J/g)).

Considering the evolution of the activation energy (E_a) and T_{peak} vs T_{max}, a jump is observed in the two curves at a temperature ranging between 925 and 975 °C (insert in Fig. 13). These jumps could be associated to a change in the "regime" of the structural mechanism and a possible phase transition towards the $P6_322$ phase, comparable to the one observed in the undoped aluminate $SrAl_2O_4$. In the latter, this transition from $P6_3$ (supercell) towards $P6_322$ (unit cell) has indeed been reported at a temperature close to 860 °C [13] on the basis of neutron diffraction refinements carried out up to 1200 °C.

6. Discussion and mechanism models

6.1. Structural models

The present TEM observations, coupled with XRPD studies, evidenced the polymorphism of $SrAl_{1.5}Fe_{0.5}O_4$ with the characterization of four different phases (Table 1). A minor phase hexagonal $P6_3$-type, observed in the form of small domains, and the stable monoclinic $P2_1$-type phase are isotypic with one of the high and the low temperature forms of the undoped $SrAl_2O_4$, respectively. In order to discuss the possible models obtained for the new O_1 and O_2-$SrAl_{1.5}Fe_{0.5}O_4$ annealed phases with regard to the H- and M-structures, a topological mode is firstly used to describe the networks, accounting only the relative orientation of the tetrahedra (“up” and “down” pointing apices of adjacent tetrahedra) and not the degree of the tetrahedra and oxygen layers distortion. In the two parent H- and M-structures, the Al/Fe tetrahedra share corners and form an honeycomb network, in which one face of each tetrahedron is almost parallel to (*a*,*b*) plane and the apical oxygen is located above or below the plane in a ‘up’ (U) or ‘down’ (D) configuration. In H- and M-structures, honeycomb rings exhibit UDUDUD configuration. Because of the close metrical relationships between H, M, O_1- and O_2-cells, especially evidenced in the ED patterns, we supposed that the tetrahedra of the O_1- and O_2-$SrAl_{1.5}Fe_{0.5}O_4$ structures adopt also a honeycomb network. Three models are retained, $P222_1$ for O_2-$SrAl_{1.5}Fe_{0.5}O_4$ and $P2_1mn$ or $P11n$ for O_1-$SrAl_{1.5}Fe_{0.5}O_4$, because of their close relationships with the parent structures and the microstructural mechanisms observed in the course of the TEM study.

The O_2-$SrAl_{1.5}Fe_{0.5}O_4$ crystallizes in an orthorhombic $P222_1$ space group, compatible with a UDUDUD configuration, as shown in Fig. 14a. The superstructure observed could be considered as the result of one “soft” relaxation mechanism, without change of the tetrahedra configuration. Theoretical images have been calculated for this ideal model. Starting from the atomic positions of this model, they provide a satisfactory agreement with the main typical features of the experimental contrast, as illustrated along [001] in Fig. 7 (insert); along [010], the strong difference in contrast, observed for certain focus values between the monoclinic matrix and the distorted zone supports the model of the O_2-$SrAl_{1.5}Fe_{0.5}O_4$ (see Fig. 3S in supplementary material for example).

The situation is more complex in the case of the O_1-structure because different structural models can be established considering the symmetry elements imposed by the possible space groups determined by ED, without unequivocal solution. The tetrahedra cannot be arranged into a honeycomb network in the Pmmn space group, since it excludes the possibility to locate a **m** mirror perpendicular to $\vec{a}$. In the orthorhombic $P2_1mn$ space group, the tetrahedra can adopt a honeycomb arrangement but, due to the presence of the **m** mirror perpendicular to $\vec{b}$, the configuration in the O_1-structure cannot be UDUDUD. A possible $P2_1mn$ configuration is shown in Fig. 14b, it exhibits the sequence UUDUUD as in $BaCaGa_4O_8$ [28]. Another possible $P2_1mn$ configuration, more unlikely with alternations of UUUUUU and UUDDDD sequences, has been discarded. If we consider the $P11n$ space group (with $\approx 90^\circ$), a possible configuration of the O_1 structure corresponds to the formation of UDUDUD and UDDUDU sequences, observed in $CaAl_2O_4$ [17,21] as shown in Fig. 14c. As for the O_2-model, calculated images have been carried out from the atomic positions of these $P11n$ and $P2_1mn$ models. The best results have been obtained for the $P11n$ model (Fig. 7), even at the level of the planar defect, contrary to the $P2_1mn$ model.

XRPD refinements have been attempted at room temperature on the annealed A_{nn} sample in which the different phases have been considered. Different constraints have been applied on profile parameters and on Al/Fe–O and Sr–O distances, but no significant result emerged for the O_1 and the O_2 structures, because of important overlaps and broadenings of the reflections. A high temperature XRPD study could maybe solve the structures of the orthorhombic models.

6.2. Polymorphic transitions in $SrAl_{1.5}Fe_{0.5}O_4$

The TEM studies of the system provide two levels of information: the possible arrangements of the tetrahedral framework by the characterization of the stabilized phases on the one hand and the structural mechanisms through the formation of the O_1- and O_2-$SrAl_{1.5}Fe_{0.5}O_4$ phases in the monoclinic matrix and their coexistence in the form of oriented nano-domains in the annealed samples and complex (TB, PD and AB) interfaces on the other hand. Based on the UDUDUD arrangement of the H- and M- mother $SrAl_{1.5}Fe_{0.5}O_4$ phases, three solutions have been retained, from the ED and image observations, for the new supercells: $P222_1$-type for the O_2-$SrAl_{1.5}Fe_{0.5}O_4$ phase and $P2_1mn$-

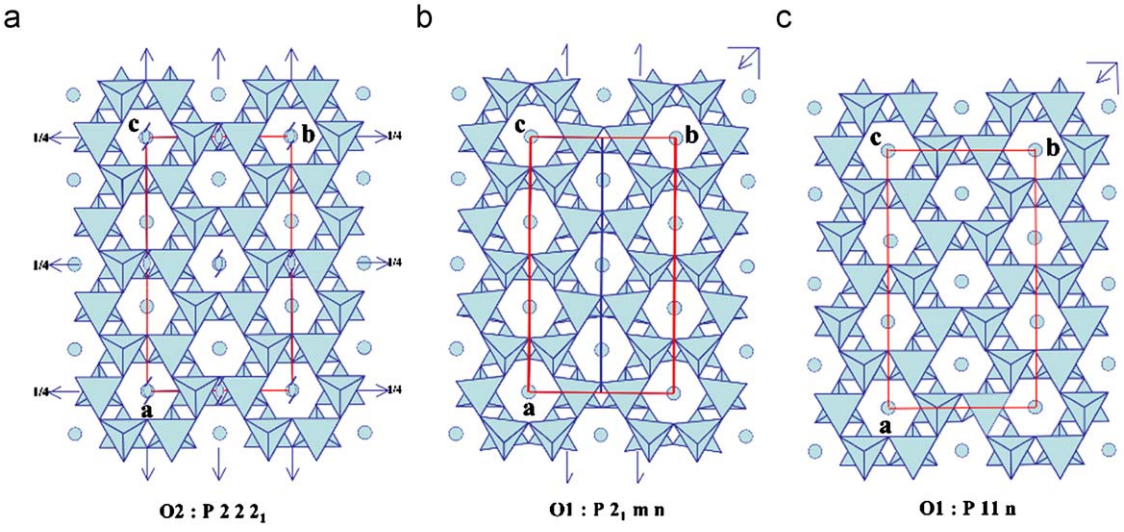

Fig. 14. Projection of the proposed models: (a) for the O_2-$SrAl_{1.5}Fe_{0.5}O_4$ phase with the $P222_1$ space group; (b) for the O_1-$SrAl_{1.5}Fe_{0.5}O_4$ phase with the $P2_1mn$ space group and (c) for the O_1-$SrAl_{1.5}Fe_{0.5}O_4$ phase with the $P11n$ space group.

or $P11n$-type for the O_1-$SrAl_{1.5}Fe_{0.5}O_4$ phase. The arrangements of the tetrahedra and Sr^{2+} cations being similar in the H-, M- and O_2-structures ($P222_1$-type), the transitions between the three structures as a function of T can be easily explained through distortion mechanisms of the tetrahedra without rearrangement of the framework (Fig. 14a).

This is not the case of the O_1-structure, whatever the space group, $P2_1mn$ (Fig. 14b) or $P11n$ (Fig. 14c). The transition between the M- and O_2-$SrAl_{1.5}Fe_{0.5}O_4$ structures implies necessarily a rearrangement of, at least, a part of the matrix. It can be explained through two basic structural units, which build the tetrahedral framework of the UDUDUD networks, only accounting the "U" or "D" orientation of the tetrahedra. The network is commonly described as being built by the condensation, via common corners, of chains "UD" parallel to $\vec{a}$. In the tridymite structure, the chains are built up from alternating "UD" tetrahedra (pink chain in Fig. 15) and, in an ideal model, parallel chains "UD" alternate along $\vec{b}$, translated by $1/2\vec{a}+1/2\vec{b}$ (from the hexagonal parent structure). The second structural units correspond to (100) slices built up of couples of alternating "up and down" (UD) tetrahedra parallel to $\vec{b}$, separated by the Sr^{2+} cations located in the cages (deep blue slice in Fig. 15). In $SrAl_2O_4$, all the slices (labelled S_{UD}) are built up of similarly oriented (UD) tetrahedra alternating along $\vec{a}$; the adjacent slices are translated by the vector $\vec{t}=1/2\vec{a}+1/2\vec{b}$ with regard to each other (in an ideal model).

In the $P2_1mn$ model of the O_1-$SrAl_{1.5}Fe_{0.5}O_4$ structure, chains "UD" parallel to $\vec{a}$ are retained. However, because of the **m** mirror, each chain alternates with its image along $\vec{b}$ at neighbour so

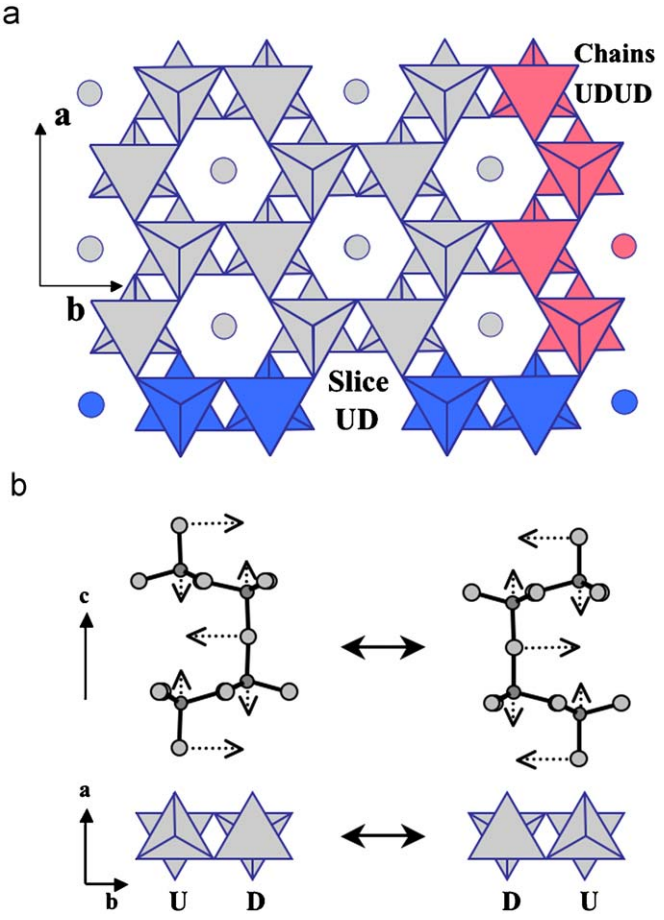

Fig. 15. (a) Drawing of the basic structural units, the chains "UD" and the slice S_{UD}, in a matrix UDUDUD of a tridymite-type structure (b) Transformation mechanism of a UD unit into a DU unit.

that they transform the tetrahedral UDUDUD ring in UUDUUD ring via their common oxygen. This structural mechanism could be associated to one of the defects (Fig. 11b), which have been observed in the monoclinic matrix in the course of the transition. The appearance of local doubling or tripling of the b_M parameter could indeed be explained through the intercalation of (010) defective "UD" chains, which play the role of antiphase boundary (AB) and transforms locally the UDUDUD arrangement in a UUDUUD. It therefore results in the formation of single $P2_1mn$-type member or of local polytypes of a few units long in the matrix. Note that these defective members exhibit easily "super-dislocations", which are associated to the local shift of the boundaries along $\vec{b}_M$ (one example is given in supplementary material, in Fig. 2S).

In the model $P11n$ of the O_1-$SrAl_{1.5}Fe_{0.5}O_4$ phase, the structure can be described from the sequence along $\vec{a}$ of three slices "DU" (S_{DU}) followed by three slices "UD" (S_{UD}). The junction between the 3 S_{DU} and 3 S_{UD} transforms the UDUDUD rings in UUDUDD rings. This model is the one that provides the best fit between the experimental and simulated images. The existence of these groups of three slices, or blocks, different of the three adjacent ones along $\vec{a}$ is also consistent with the contrast observed in the (100) planar defects, which systematically appear in the form of three rows of a peculiar contrast.

In the two examples of structural mechanisms, an inversion of the configuration (U)/(D) of the tetrahedra is observed in the chains or in the couples of tetrahedra of the slices. Two adjacent columns of $(Al,Fe)_2O_7$ groups having a "UD" configuration can adopt the inverse configuration through a joint displacement of the Al(Fe) and connecting oxygens along $\vec{c}$. In the H-, M- or O_2-type matrices, the inversion of one (010) chain induces the transition toward domains of $P2_1mn$-type (O_1-$SrAl_{1.5}Fe_{0.5}O_4$ structure), as observed in Fig. 12. A similar mechanism of inversion, which occurs in three (100) slices (UD) out of six, induces the transition toward domains of $P11n$-type (O_2-$SrAl_{1.5}Fe_{0.5}O_4$ structure), as observed in Fig. 11b. Through this mechanism, the O_2-$SrAl_{1.5}Fe_{0.5}O_4$ structure can be described by the alternation of blocks of three (S_{UD}) and three (S_{DU}) slices along $\vec{a}$; this description is reinforced by the TEM observations.

Interestingly, following that description in terms of basic structural (S_{UD}) and (S_{DU}) units, $KLiBeF_4$ exhibits the hexagonal structure (UDUDUD) built of a single type of (S_{UD}) slices while NH_4LiBeF_4 can be described [29] by the existence of sheets built up of alternating single slices (S_{UD})/(S_{DU}) (with the equivalent parameter $a=A$), leading to an UUUDDD arrangement. In the same way, the β-$SrGa_2O_4$ [30] can be described by the existence of sheets built up of alternating double slices (S_{UD}) and double (S_{DU}), leading to an UUDUDD arrangement; this structure is characterized by UUD-type chains and the $P2_1/c$ space group (with the equivalent parameter $a=2A$). The β-$SrGa_2O_4$ can be described by the alternation of blocks of two (S_{UD}) and two (S_{DU}) slices along $\vec{a}$. This compound also exhibits a transition towards a γ-$SrGa_2O_4$ structure, characterized by a modification of the relative orientation of the (D) and (U) pointing apices of adjacent tetrahedra, which involves the alternation of single slices (S_{UD})/(S_{DU}) along $\vec{a}$.

As previously outline, these topological models do not account the distortion of the oxygen coordination spheres and the puckering of the equatorial oxygen atoms of the layers, which are also responsible of the lowering of the symmetry. They are associated to the variation of the position of one of the basic structural units, either along $\vec{b}_M$ (the chains "UD" of tetrahedra) or $\vec{a}_M$ (the slice of double tetrahedra S_{UD} or S_{DU}). One can therefore consider that these structures are likely playing an important role in the non-stoichiometry mechanisms observed along $\vec{b}_M$ and $\vec{a}_M$ in the different samples, as observed in the TEM images.

Such mechanisms are favourable to topotactic processes. Starting from the UDUDUD arrangement of the high temperature

form, one can assume that the lowering in symmetry observed at low temperature induced important strains in the framework, which could be released by different mechanisms leading to stuffed superstructures:

by retaining the UDUDUD blocks (as in the supercell $P222_1$ of the O_2-structure)

by the formation of sheets in the $P11n$ model (built up of two different rings UDUDUD and UUDUDD)

by the formation of antiphase-like boundaries which involve the formation of polytypes, starting point toward the $P2_1mn$ model (built up of a single ring UUDUUD).

The observations of a spectacular "pseudo-hysteresis", which exhibits an ultra broad transition with $\Delta T \approx 500\,^{\circ}C$ as T increases and rather sharp one $\Delta T \approx 10\,^{\circ}C$ as T decreases, can be explained considering the TEM observations. Two possible effects could be combined to propose an explanation to such behaviour.

1. The first one deals with the doping effect of iron, which is important. We saw that the introduction of iron allows to stabilise the $P2_1$ isotype at a lower synthesis temperature than the one needed for the undoped phase. Moreover, it involves additional transformations of the basic cell. Consequently, despite the EDS analyses showed that the cation deviations with regard to the average composition are in the limits of the techniques accuracy, the tiny local composition variations of the "randomly" distributed Fe and Al atoms in the tetrahedral could be an important parameter.
2. The second deals with the topotactic process evidenced by the TEM techniques, which involves a complex microstructural state of the material with the coexistence of the different forms, down to the nanoscale level. The different nanophases are trapped and the transition toward the high T form would therefore need energy for overcoming the resulting constrains.

The combination of two effects, firstly the microstructural state (and pinning of the nanostructures) and, second, the tiny variations of the iron content, which could act on the first state, could be sufficient to explain the broad transition observed by increasing the annealing temperature. The more high is this temperature, the more the homogeneous high T form is restored; therefore, the more important is the fraction of the high T form, the more intense would be the signal of the transition HT→LT toward the ordered phases observed by decreasing T.

7. Concluding remarks

Four different phases have been characterized at room temperature by TEM, XRPD and DSC techniques in the stuffed tridymite structures of $SrAl_{1.5}Fe_{0.5}O_4$. The H-$SrAl_{1.5}Fe_{0.5}O_4$ phase, stable at high temperature, is trapped by the monoclinic structure during a rapid decrease of the temperature. The M-$SrAl_{1.5}Fe_{0.5}O_4$ phase is very stable and can be stabilised by cooling the hexagonal form, whatever the cooling rate. The structure refinement from XRPD data shows that each layer perpendicular to $\vec{c}$ is made of rings of six tetrahedra, according to the sequence UDUDUD, without any preferential occupancy of iron in one of the four tetrahedral sites. The original superstructures O_1- and O_2-$SrAl_{1.5}Fe_{0.5}O_4$ have been systematically observed concomitantly and intimately intergrown. The TEM analyses suggest that the transition between the four different phases follow topotactic mechanisms, through the formation of twinning boundaries, antiphase boundaries and planar defects, which are all coherent, and can be easily translated in the matrix. One important point of the TEM analyses is to show that the transition HT→LT is dynamic and that the microstructure of each of the samples is strongly dependent of the thermal history. This could be one of the keys of the aforementioned controversy on the mechanism transition between the $P2_1$, $P6_3$ and $P6_{322}$ structures of $SrAl_2O_4$. Note that similar studies are carried out on the $P6_3$ and $P6_{322}$ structures of $BaAl_2O_4$ (UDUDUD arrangement) and a recent paper [31] shows that the $P6_3$ structure would not be correct on the local scale.

The annealed (A_{nn}) sample exhibits a mesomorph state, characterized by the coexistence of the two O_1- and O_2-$SrAl_{1.5}Fe_{0.5}O_4$ phases having the same composition and the same parameters but different symmetries. A reversible transition is observed from this semi-ordered state to a crystalline phase. This dynamic transition LT→HT takes place over a very wide temperature range from 620 to 1120 °C. The reversibility of the transition (HT→LT) is confirmed by the DSC measurements and diffraction techniques. The crystallization energy of the orthorhombic phases is of the order of 10 J/g, consistent with the values commonly observed and characterized by a single peak at $T \approx 623\,^{\circ}C$ as T decreases. The peculiar behaviour deals with the variation of the peak height observed as the T_{MAX} of annealing increases, explained by the complex microstructures, which create an ill-defined energy barrier.

Appendix A. Supplementary material

Supplementary data associated with this article can be found in the online version at doi:10.1016/j.jssc.2009.04.013.

References

[1] T.J. Mazanec, R. Prasard, R. Odegard, C. Steyn, E.T. Robinsonn, Stud. Surf. Sci. Catal. 136 (2001) 147.
[2] W.C. Hansen, L.T. Brownmiller, R.H. Bogue, J. Am. Chem. Soc. 50 (1928) 396.
[3] A.A. Colville, S. Geller, Acta Cryst. B 27 (1971) 2311.
[4] A.A. Colville, S. Geller, Acta Cryst. B 28 (1972) 3196.
[5] J.G. Redhammer, G. Tippelt, G. Roth, G. Amthauer, Am. Mineral. 89 (2–3) (2004) 405.
[6] J.Y. Lee, J.S. Swinnea, H. Steinfink, W.M. Reiff, S. Pei, J.D. Jorgensen, J. Solid State Chem. 103 (1993) 1.
[7] H.K. Muller Buschbaum, J. Alloys Compd. 349 (2003) 49.
[8] G. Blasse, A. Bril, Philips Res. Rep. 23 (1968) 201.
[9] A.R. Schulze, H. Mueller-Buschbaum, Z. Anorg. Allg. Chem. 475 (1981) 205.
[10] K. Fukuda, K. Fukushima, J. Solid State Chem. 178 (2005) 2709.
[11] S. Ito, S. Banno, K. Suzuki, M. Igani, Z. Phys. K. Neue Folge 105 (1977) 173.
[12] U. Rodehorst, M.A. Carpenter, S. Marion, C.M.B. Henderson, Mineral. Mag. 67 (2003) 989.
[13] M. Avdeev, S. Yakovlev, A.A. Yaremchenko, V.V. Kharton, J. Solid State Chem. 180 (2007) 3535.
[14] P. Berthet, J. Berthon, C. Heger, A. Revcolevschi, Mater. Res. Bull. 27 (1992) 919.
[15] V. Kahlenberg, R.X. Fischer, Solid State Sci. 3 (2001) 433.
[16] E.M. Levin, C.R. Robbins, H.F. Mc Murdie, Phase Diagrams for Ceramists, vol. 6, Ed. American Ceramic Society, USA, 1964.
[17] V. Kahlenberg, Eur. J. Mineral. 13 (2001) 403.
[18] A.A. Yaremcheko, V.V. Kharton, A.A. Valente, A.L. Shaula, F.M.B. Marques, J. Rocha, Solid State Ionics 177 (2006) 2285.
[19] A.V. Kovalevsky, V.V. Kharton, F. Maxim, A.L. Shaula, J.R. Frade, J. Membr. Sci. 278 (2006) 162.
[20] A.V. Kovalevsky, V.V. Kharton, F.M.M. Snijkers, J.F.C. Cooymans, J.J. Luyten, J.R. Frade, Solid State Ionics 179 (2008) 61.
[21] W. Hörkner, H.K. Müller-Buschbaum, J. Inorg. Nucl. Chem. 38 (1976) 983.
[22] T. Lehnert, S. Crevoiserat, R. Gotthardt, J. Mater. Sci. 37 (2002) 1523.
[23] K. Jacobs, P. Hofmann, D. Klimm, J. Reichow, M. Schneider, J. Solid State Chem. 149 (2000) 180.
[24] C. Dodinh, E.F. Bertaut, Bull. Soc. Fr. Mineral. Cristallogr. 88 (1965) 413.
[25] S.Y. Huang, R. von der Mühll, J. Ravez, J.P. Chaminade, P. Hagenmuller, M. Couzi, J. Solid State Chem. 109 (1994) 97.
[26] A.M. Abakumov, O.I. Lebedev, L. Nistor, G. van Tendeloo, S. Amelinckx, Phase Transitions 71 (2000) 143.
[27] P. Armand, M. Beaurain, B. Ruffle, B. Menaert, D. Balitsky, S. Clement, P. Papet, J. Cryst. Growth 310 (2008) 1455.
[28] S. Kubota, H. Yamane, M. Shimada, Acta Cryst. C 55 (1999) 14.
[29] J. Le Roy, S. Aléonard, Acta Cryst. B 28 (1972) 1383.
[30] V. Kahlenberg, R.X. Fischer, C.S.J. Shaw, J. Solid State Chem. 153 (2000) 294.
[31] A.K. Larsson, R.L. Withers, J.M. Perez-Mato, J.D. Fitz Gerald, P.J. Saines, B.J. Kennedy, Y. Liu, J. Solid State Chem. 181 (2008) 1816.